

ARTICLE

Open Access

Formation of binary magnon polaron in a two-dimensional artificial magneto-elastic crystal

Sudip Majumder¹, J. L. Drobitch², Supriyo Bandyopadhyay² and Anjan Barman¹ 

Abstract

We observed strong tripartite magnon-phonon-magnon coupling in a two-dimensional periodic array of magnetostrictive nanomagnets deposited on a piezoelectric substrate, forming a 2D magnetoelastic “crystal”; the coupling occurred between two Kittel-type spin wave (magnon) modes and a (non-Kittel) magnetoelastic spin wave mode caused by a surface acoustic wave (SAW) (phonons). The strongest coupling occurred when the frequencies and wavevectors of the three modes matched, leading to perfect phase matching. We achieved this condition by carefully engineering the frequency of the SAW, the nanomagnet dimensions and the bias magnetic field that determined the frequencies of the two Kittel-type modes. The strong coupling (cooperativity factor exceeding unity) led to the formation of a new quasi-particle, called a binary magnon-polaron, accompanied by nearly complete (~100%) transfer of energy from the magnetoelastic mode to the two Kittel-type modes. This coupling phenomenon exhibited significant anisotropy since the array did not have rotational symmetry in space. The experimental observations were in good agreement with the theoretical simulations.

Introduction

Magnon-phonon coupling in two-dimensional artificial magnetoelastic “crystals” (two-dimensional periodic arrays of magnetostrictive nanomagnets fabricated on a piezoelectric substrate) is an active area of research^{1–28}. Coherent magnons have been excited in magnets by broadband coherent phonon wave packets, localized monochromatic phonons, and propagating surface acoustic waves^{9,26,28}. More recently, when the coupling between magnons and phonons is sufficiently strong, they were found to spawn a new quasi-particle, called the *magnon-polaron*^{1,2,8–14}.

When a two-dimensional artificial magnetoelastic crystal (2D-AMEC) is placed in a magnetic field and an acoustic wave is launched in the piezoelectric substrate, three different types of spin wave modes can be excited. The first is the *Kittel mode*^{27,29}, which is associated with

spin precession about the magnetic field. The frequency of this type of spin wave increases with the strength of the magnetic field in accordance with the Kittel formula²⁹. The second type is observed even when no magnetic field is present^{22,30,31}. In this case, the spin precession is caused by the periodic strain due to the acoustic wave. It can only be observed in magnetostrictive nanomagnets since it requires magnetoelastic coupling. The frequency of this mode is independent of the magnetic field since it does not have a magnetic origin and is usually the same as the frequency of the acoustic wave. The two types can hybridize to generate the third type, called the hybrid magneto-dynamical modes⁶, whose frequencies increase with the magnetic field but do not obey the Kittel formula.

A probe of spin wave modes usually begins with a two-color time-resolved magneto-optical Kerr effect (TR-MOKE)^{32,33} measurement to extract the temporal magnetization oscillations in the nanomagnets. These oscillations are measured at different magnetic fields and then Fourier transformed to obtain the power spectrum at every magnetic field. At any given magnetic field, there are typically multiple peaks in the spectrum, with each

Correspondence: Anjan Barman (abarman@bose.res.in)

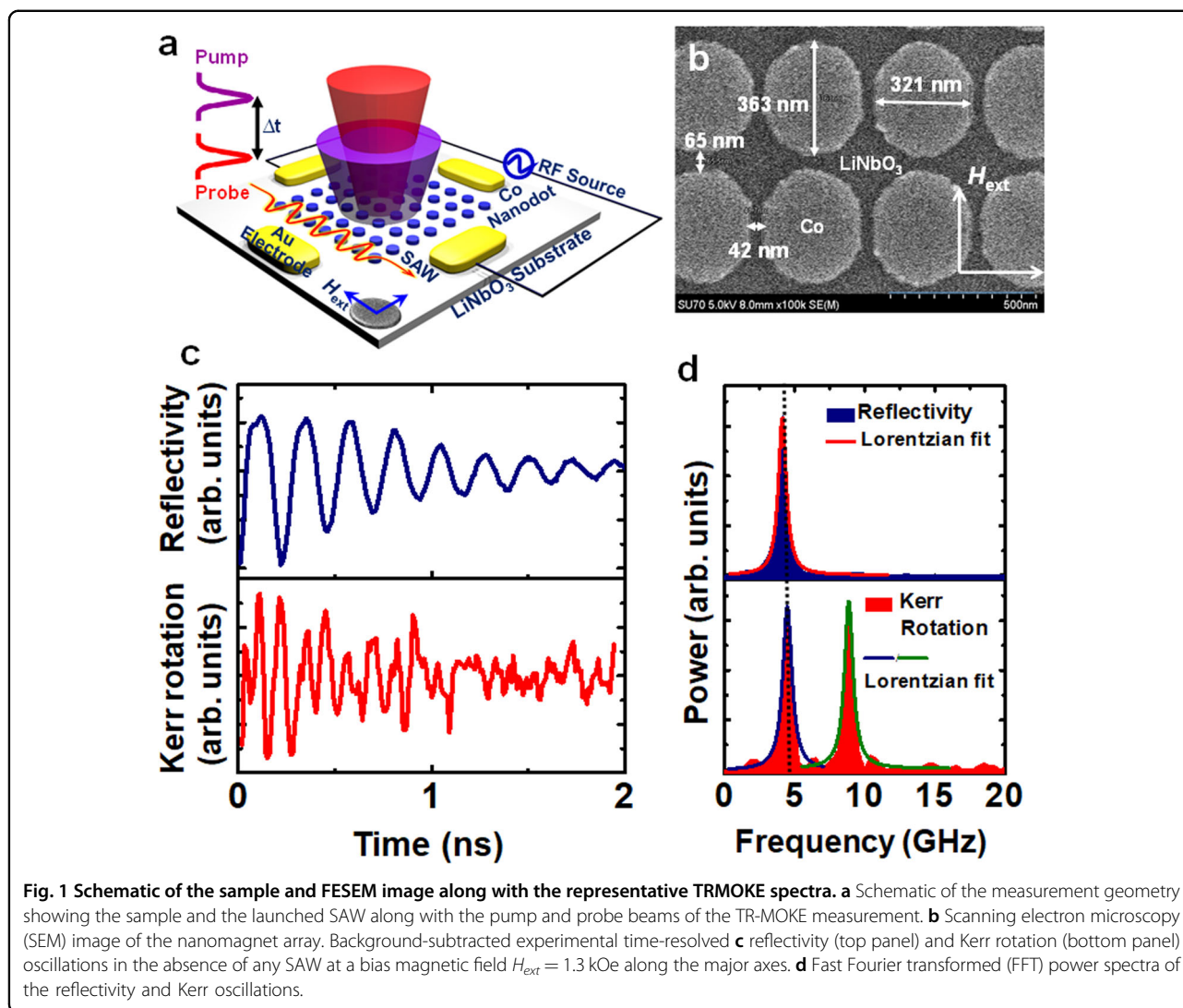
¹Department of Condensed Matter and Materials Physics, S. N. Bose National Centre for Basic Sciences, Block JD, Sector-III, Salt Lake, Kolkata 700 106, India

²Department of Electrical and Computer Engineering, Virginia Commonwealth University, Richmond, VA 23284, USA

© The Author(s) 2023



Open Access This article is licensed under a Creative Commons Attribution 4.0 International License, which permits use, sharing, adaptation, distribution and reproduction in any medium or format, as long as you give appropriate credit to the original author(s) and the source, provide a link to the Creative Commons license, and indicate if changes were made. The images or other third party material in this article are included in the article's Creative Commons license, unless indicated otherwise in a credit line to the material. If material is not included in the article's Creative Commons license and your intended use is not permitted by statutory regulation or exceeds the permitted use, you will need to obtain permission directly from the copyright holder. To view a copy of this license, visit <http://creativecommons.org/licenses/by/4.0/>.



corresponding to a mode at that magnetic field. When these peaks are plotted versus the magnetic field, one obtains different *branches*, with each representing a mode that can be of type 1, 2 or 3. When two branches avoid crossing each other at the point of intersection, coupling between their corresponding modes occurs. This coupling can occur between modes of the same type or two different types. It is also possible that a third mode mediates the coupling between two other modes. In this last case, avoided crossing occurs at the confluence of the three branches corresponding to the three modes. Here, we report this kind of tripartite coupling where a magnetoelastic mode (type 2 mode) mediates coupling between two hybrid magnetodynamical modes (type 3 modes).

The strength of the coupling between the two modes is gauged in the following way. The avoided crossing causes a frequency gap Δf at the point of the avoided intersection. The coupling rate is define as $g = \Delta f/2$, and the

cooperativity factor is defined as $C = g^2/\kappa_1\kappa_2$, where κ_1 is the loss rate of one mode and κ_2 is that of the other mode¹. The latter two quantities are approximately the linewidths of the spectral peaks corresponding to the two modes at a magnetic field sufficiently far away from the point of the avoided crossing where each mode is uncoupled to the other and therefore preserves its own character. A value of $C > 1$ and $g > \kappa_1, \kappa_2$ indicates strong coupling.

Results and discussion

Figure 1a shows the schematic of the sample used in our study and the TR-MOKE measurement setup. The sample consists of 6-nm-thick elliptical Co nanomagnets with major and minor axes of dimensions of 363 nm and 321 nm fabricated on a LiNbO₃ substrate. The nanomagnet's lateral dimensions and pitch are shown in the scanning electron micrograph of Fig. 1b. Surrounding the nanomagnet array

are solid rectangular electrodes that are used to launch a SAW in the substrate. Antipodal electrode pairs are a few mm apart. By selecting which antipodal electrode pairs are activated (by applying a sinusoidal voltage between them), we can choose the direction in which the SAW propagates. Here, we have used solid electrodes instead of the usual interdigitated transducers (IDTs), thereby sacrificing some SAW coupling efficiency because the IDTs act as narrow-band filters and are ineffective at frequencies far from their resonant frequencies. Since the SAW frequencies that will result in the strongest tripartite coupling are not known a priori, we have to launch SAWs covering a broad spectrum of frequencies; hence, there is no specific frequency to design the IDTs. Therefore, we cannot use IDTs and must use solid electrodes that are broadband launchers and enable the launching of a wide spectrum of SAW frequencies, albeit with lower conversion efficiencies. We emphasize that we do not launch a broadband SAW with these electrodes. Instead, we launch monochromatic SAWs, but we are able to vary the SAW frequency over a wide spectrum, which could not have been accomplished with IDTs.

The SAWs that are launched in our samples are very different from the traditional Rayleigh, Sezawa, Lamb or Love modes because of the nature of the launching electrodes. When a time-varying voltage is applied between any two antipodal electrodes (Fig. 1a), a time-varying strain is produced in the region pinched between these electrodes owing to d_{31} and d_{33} coupling in the piezoelectric substrate (<https://www.researchgate.net/post/What-is-the-difference-between-d33-d31-d32-component-of-piezoelectric-coefficient>). The time-varying strain produces an acoustic wave whose wavelengths at the frequencies of interest are several orders of magnitude smaller than the separation between the antipodal electrodes. Hence, we can disregard confinement (cavity) effects and view the acoustic wave as a propagating (unconfined) wave instead of a standing wave. The electrodes are fabricated with e-beam evaporation and diffuse $<1 \mu\text{m}$ into the piezoelectric substrate. At the frequencies used, the wavelengths of the acoustic waves are smaller than $1 \mu\text{m}$ and much smaller than the substrate thickness. Consequently, these waves do not deeply penetrate into the substrate but remain confined near the surface. Thus, we loosely call them “surface acoustic waves” (SAWs). The nature of these waves is discussed in the supplementary section of ref. ³. Since the line joining the centers of the opposite electrodes in Fig. 1a is either parallel to the major axis of the nanomagnets or the minor axis, the SAW propagates either parallel to the major axis or the minor axis, depending on which pair is activated.

The ultrafast magnetization dynamics in the nanomagnets in the presence of a SAW in the substrate and an external bias magnetic field were measured with a custom-built TR-MOKE microscope in a collinear two-color pump–probe setup. The second harmonic ($\lambda = 400 \text{ nm}$, spot size $\sim 1 \mu\text{m}$, pulse width $\sim 100 \text{ fs}$,

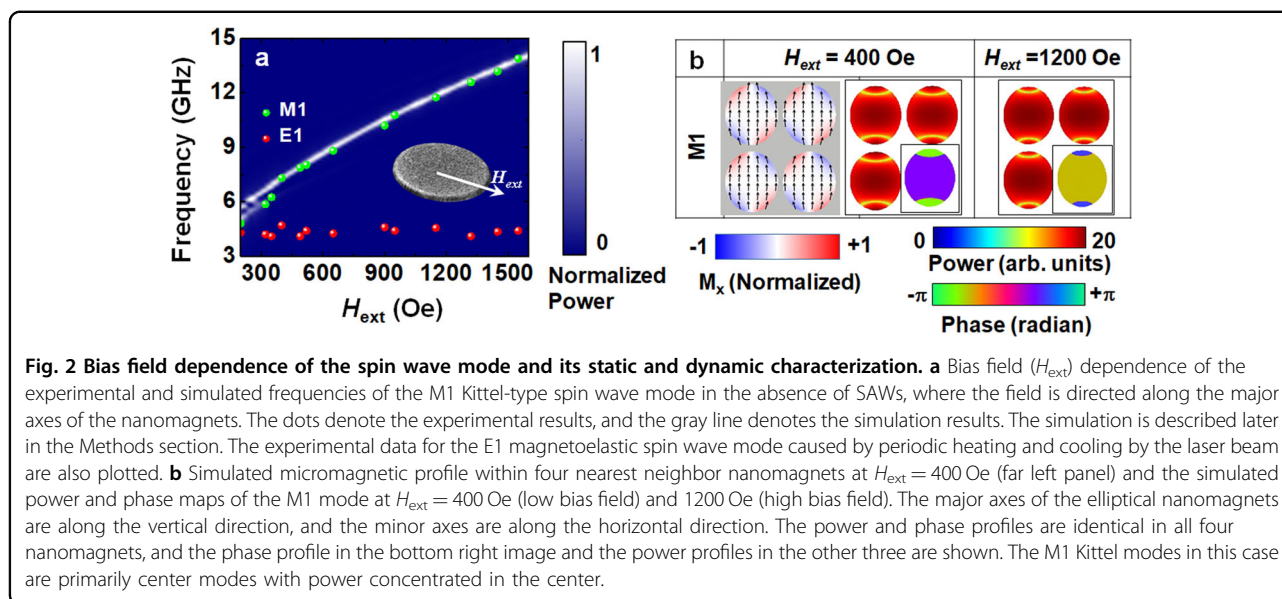
fluence $\sim 12 \text{ mJ cm}^{-2}$) of a Ti sapphire oscillator was used to excite the dynamics, whereas a time-delayed fundamental laser ($\lambda = 800 \text{ nm}$, spot size $\sim 800 \text{ nm}$, pulse width $\sim 80 \text{ fs}$, fluence $\sim 1 \text{ mJ cm}^{-2}$) was used to probe the dynamics. The probe beam spot covers approximately four nanomagnets since the lateral dimensions of the nanomagnets are $\sim 350 \text{ nm}$ and the edge-to-edge spacing is 65 nm vertically and 42 nm horizontally. Hence, four nanomagnets are always simultaneously probed.

Magnetodynamics in the absence of any SAW

We first interrogate the nanomagnet array with TR-MOKE in the absence of any SAW to probe the intrinsic spin wave modes and dynamics in the presence of a bias magnetic field H_{ext} . The measured time-resolved reflectivity and Kerr rotation signals are obtained with H_{ext} directed along the major axes of the elliptical nanomagnets (magnetic easy axis) and are shown in Fig. 1c at $H_{\text{ext}} = 1.3 \text{ kOe}$. The fast Fourier transformed (FFT) power spectra of the reflectivity and the Kerr rotation oscillations are shown in Fig. 1d. The experimental spin wave spectrum (spectrum of the Kerr oscillation) shows two distinct modes. Among them, one mode (M1), occurring at the higher frequency, is either type 1 or type 3 since its frequency was found to increase with an increasing bias magnetic field. The continuous SW branches present are fitted using the Kittel formula for SW frequency (f) as shown below:

$$f = \frac{\gamma}{2\pi} \sqrt{(H_{\text{ext}} + H_{\text{ani}})(H_{\text{ext}} + H_{\text{ani}} + 4\pi M_{\text{eff}})}, \quad (1)$$

where γ , M_{eff} and H_{ani} are the gyromagnetic ratio, the effective magnetization, and the anisotropy field, respectively. From the Kittel fit of M1, the extracted value of saturation magnetization M_{s} is determined to be 1080 emu/cc assuming the Landé g -factor $g = 2$ in the calculation of the gyromagnetic ratio. This value is slightly less than the value of 1400 emu/cc for bulk cobalt; however, this is reasonable since these are *nanomagnets* of cobalt and unsaturated magnetization can be present in the periphery of the nanomagnets. Hence, this appears to be the type 1 or pure (Kittel type) magnetic mode. The Kittel fit of spin wave frequency is represented in the Supplementary Material. Details of the fit are described in Section S1 of the Supplementary Material. The lower frequency mode (E1), appearing at 4.1 GHz , has magnetic-field-independent frequency and is, hence, a magnetoelastic mode (type 2). This was also observed in the time-resolved reflectivity signal, as shown in Fig. 1d. We also observed this type of mode in previous studies³, and this mode was clearly not caused by any *externally applied* SAW since none was launched. Instead, this mode was caused by an acoustic wave that was generated by the



periodic heating and cooling of the substrate by the laser, which produced a periodic strain in the substrate owing to periodic thermal expansion and contraction of the nanomagnets and the substrate. The strain occurred because the thermal expansion/contraction coefficients of the nanomagnets and the substrate were unequal. This type of laser-induced acoustic wave was observed by others²². The associated periodic strain excited the magnetization precession in the magnetostrictive nanomagnets owing to the inverse magnetostriction (Villari) effect and caused the E1 mode to appear.

The bias magnetic field dependence of the two observed modes (E1 and M1) is shown in Fig. 2a. Here, experimental data are plotted as points, and the gray line represents the results of micromagnetic simulations described later in the Methods section (for mode M1 only). Only at sufficiently high magnetic fields (>250 Oe) can the two branches be clearly resolved, and they diverge from each other, as shown in Fig. 2a. At lower magnetic fields (<250 Oe), the two branches are too close to each other to be unambiguously resolved. The frequency of E1 remains independent of the magnetic field (type 2 behavior); however, the frequency of M1 increases with an increasing magnetic field, and it increases in accordance with the Kittel formula, indicating that it is a type 1 mode.

As stated earlier, the probe beam has a diameter of 800 nm and interrogates four nanomagnets in our samples. The calculated static spin textures within four nearest neighbor nanomagnets covered by the probe spot at a bias field H_{ext} of 400 Oe are shown in Fig. 2b, where the field is directed along the major axes of the nanomagnets. The calculations are carried out with the micromagnetic simulator Mumax3³⁴. The spins are primarily aligned along the major (easy) axes because of the

shape anisotropy of the nanomagnet, as well as the external bias field along that direction. Using the in-house software *Dotmag*³⁵, which calculates the power and phase profiles of the spin wave modes generated within a nanomagnet at different bias magnetic fields, we studied the mode profile of the M1 mode within the four neighboring nanomagnets that are interrogated by the probe beam. In Fig. 2b, we show the spatial distribution of the power and the phase profiles of M1 at two different bias field values H_{ext} of 400 Oe (low field) and 1200 Oe (high field). At both fields, the power of SW mode M1 is concentrated at the center of the nanomagnet, which signifies a uniform precessional mode.

Magnetodynamics in the presence of externally launched SAWs

In the presence of an externally launched SAW (launched by activating two antipodal electrode pairs), the magnetodynamics significantly change. Because the nanomagnet array does not have rotational symmetry as the major and minor axis dimensions of the nanomagnets are different, as are the edge-to-edge spacing along the rows and columns, we expect to observe differences depending on whether the SAW is propagating along the major axis or the minor axis³. Thus, both cases are studied.

SAW propagating along the minor axes of the elliptical nanomagnets

To launch a longitudinal SAW propagating along the minor axis of the nanomagnets, we activated an antipodal electrode pair (Fig. 1a) by applying a high-frequency voltage between them with a microwave source. The line joining the centers of this pair was aligned along the

minor axis of the nanomagnets. This caused a time-varying strain between this pair owing to d_{33} coupling in the piezoelectric substrate. The time period of the high-frequency voltage was (in all cases) longer than the piezoelectric response time of the substrate (which was ~ 60 ps); hence, the strain could follow the signal quasi-statically, meaning that the SAW frequency was approximately the same as the signal frequency with negligible phase lag. The frequency was varied while keeping the input power P fixed at +12 dBm (16 mW).

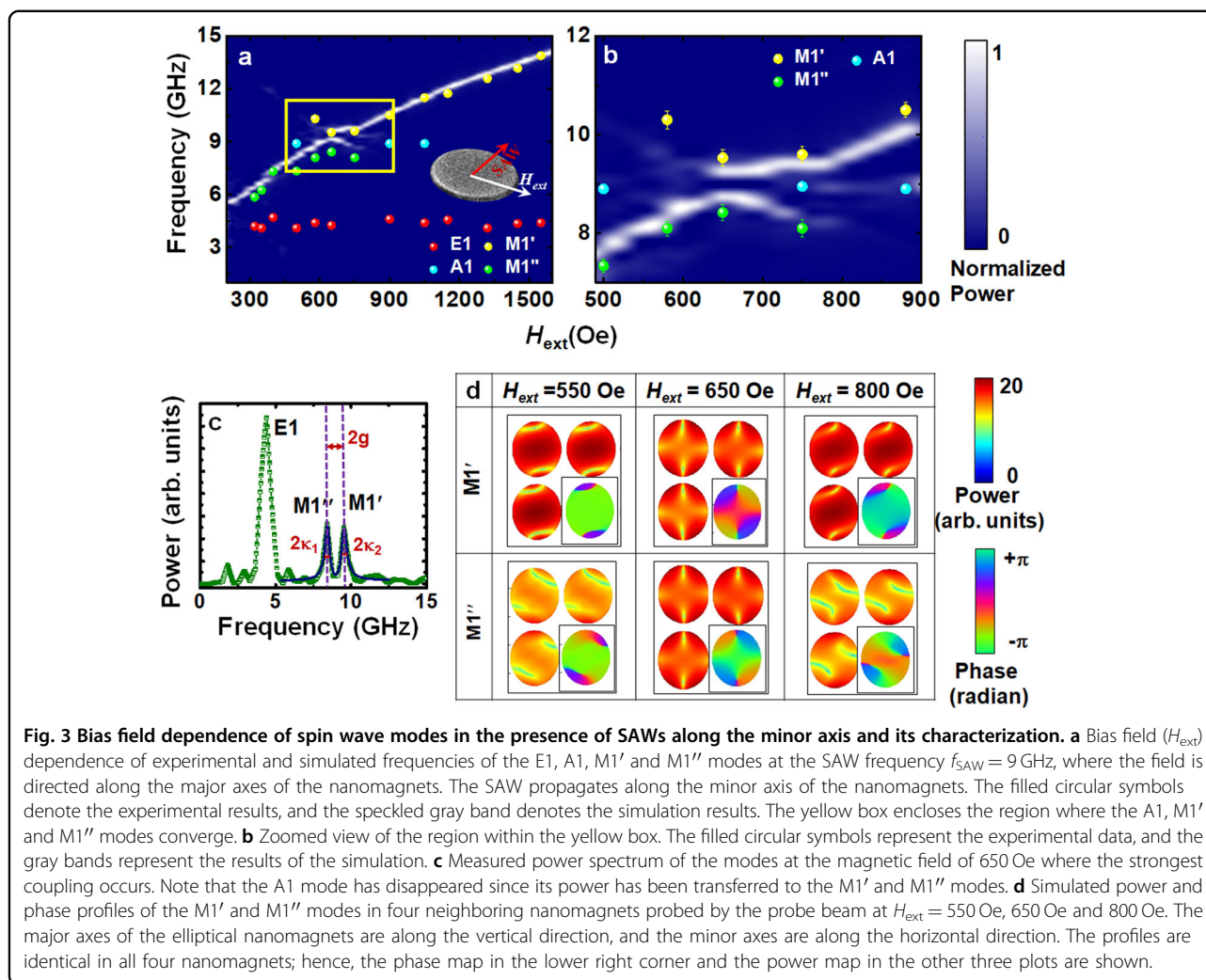
Because of the impedance mismatch between the microwave source and the sample, most of the input power was actually reflected back into the source, and only a small fraction was coupled into the piezoelectric substrate to launch the SAW. Earlier, we measured the S_{11} scattering parameter with a vector network analyzer up to 2.5 GHz⁵. Since we did not measure it across the entire frequency range of interest in this study, we did not know the power coupled into the SAW at every frequency. However, since we made only qualitative comparisons between theory and experiment, we assumed that the average S_{11} parameter in the frequency range of interest was -0.2 dB (based on the data in ref. ⁵), which meant that only $\sim 4.5\%$ of the incident power was being launched into the sample. In other words, the power coupled into the SAW (assuming all of the launched power was converted to SAW power) was ~ 0.72 mW. The actual power could potentially be somewhat different from this since the S_{11} values at the actual measurement frequencies were unknown.

As usual, we measured the time-dependent Kerr oscillations with TR-MOKE and Fourier transformed them to search for peaks that corresponded to the distinct modes. When the SAW frequency (or signal frequency) was 9 GHz, (for other SAW frequencies, see Section S3 of the Supplementary Material) four different modes E1, A1, M1' and M1'' were observed, with the first two being magnetic field independent (hence type 2 magnetoelastic modes) and the last two being magnetic field dependent (type 1, as indicated from the magnetic parameters extracted from the Kittel fit). We could actually fit the magnetic field dependences of the frequencies of the last two modes quite well with the Kittel formula assuming a g -factor of 2 and saturation magnetization M_s values of 1143 and 1155 emu/cc, respectively; the Kittel fit of spin wave frequency and details of the fit are presented in Section S1 of the Supplementary Material. Therefore, these modes had the character of Kittel modes. The M1'' mode appeared only at a low magnetic fields (< 800 Oe), whereas the M1' mode appeared only at high magnetic fields (> 600 Oe). Both modes coexist between 600 Oe and 800 Oe. Mode E1 was the same as that observed in the absence of the SAW and was caused by the periodic heating and cooling by the laser. Mode A1, on the other

hand, had the *same frequency* as that of the SAW (9 GHz); thus, it was an extrinsic magnetoelastic mode that was *directly caused by the SAW* and was not present without the SAW (which was not observed in the absence of the SAW).

Figure 3a shows the experimentally observed magnetic field dependences of the frequencies of the four modes E1, A1, M1' and M1'' when the SAW frequency f_{SAW} is 9 GHz. The points represent the experimental data, and the gray lines represent the results of micromagnetic simulations. The yellow box bounds the region where modes A1, M1' and M1'' converge; the FFT power spectra of the experimental spin wave frequencies are presented in Section S2 of the Supplementary Material. The modes converge at the frequency of the A1 mode, which is magnetic field independent, and is the SAW frequency of 9 GHz. At that frequency, there is clear avoided crossing between the branches representing modes M1' and M1'', showing that they have coupled. The phonons in the SAW, producing mode A1, act as intermediaries to couple the magnons in M1' and M1''. This result can be viewed as *tripartite* magnon-phonon-magnon coupling. In the next paragraph, we explain why this tripartite coupling cannot be observed at any arbitrary SAW frequency and magnetic field but can be observed only at specific frequencies and magnetic fields that depend on the nanomagnet dimensions.

The bias magnetic field strength where the frequencies of both M1' and M1'' come close to each other, resulting in strong coupling, is 650 Oe. This magnetic field strength is where the frequencies of both M1' and M1'' are close to 9 GHz, which is the launched SAW frequency. Figure 3c shows the power spectrum measured at this field. The frequency of M1' is slightly above 9 GHz and that of M1'' is slightly below 9 GHz in this field. The most striking feature from this figure is that the peak due to the A1 mode *vanished*, showing that its power was fully transferred to M1' and M1''. This was *complete* or *near-complete mode conversion* from the type 2 (magnetoelastic) mode A1 to type 1 (Kittel) modes M1' and M1''. The strong tripartite coupling resulted in very efficient (nearly 100%) conversion from a magnetoelastic mode to Kittel modes at this specific frequency of 9 GHz. This was possible because the *near perfect phase matching* between the magnetic field-independent A1 mode and the magnetic field-dependent Kittel-type spin wave modes M1' and M1'' occurred when their frequencies *and wavevectors* matched. This delicate matching could be ensured by three possibilities: (1) the launched SAW frequency, (2) the magnetic field, and (3) the nanomagnet dimensions (see Section S4 of the Supplementary Material). These three quantities must be carefully engineered to ensure simultaneous frequency and wavevector matching of all three modes. For fixed nanomagnet dimensions, there



could be more than one magnetic field and more than one SAW frequency where this perfect phase matching could occur.

According to coupled mode theory, 100% energy transfer is possible under perfect phase matching^{36,37}. We have carefully engineered the nanomagnet dimensions, the SAW frequency and the magnetic field (which determines the frequencies of modes M1' and M1'') to achieve the condition where both the frequencies and the wavevectors of all three modes, A1, M1' and M1'', match, leading to nearly perfect phase matching and the strong coupling. This is discussed in Section S4 of the Supplementary Material.

The mode splitting strength $2g$ where the two branches M1' and M1'' come closest in Fig. 3b is 1.11 ± 0.033 GHz. We have extracted the spectral linewidths of the M1' and M1'' modes at magnetic fields of 800 Oe and 550 Oe, respectively; these magnetic fields are farther away^{1,9,38} from the critical field of 650 Oe. Therefore, in these fields, each of the two modes has its own character. The spectral widths

have values of $\kappa_1 = 0.43 \pm 0.016$ GHz and $\kappa_2 = 0.44 \pm 0.021$ GHz, which yield a value of the cooperative factor C (defined as $C = g^2/\kappa_1\kappa_2$) of ~ 1.60 . In the avoided crossing regime, the modes lose their individual characteristics and become coupled modes with identical linewidths, and the expression for cooperativity becomes $C = g^2/\kappa^2$, which is found to be ~ 1.41 ($g = 0.565 \pm 0.033$ GHz, $\kappa \sim 0.475$ GHz) in this case. Both these cooperativity values, as well as the coupling strength and linewidth, indicate that the coupling between M1' and M1'' mediated by A1 occurs in the *strong coupling* regime, where A1 transfers all of its power to M1' and M1''. The strong tripartite coupling between two magnons (M1' and M1'') and a phonon via magnetoelastic mode A1 can be viewed as the formation of a new quasi-particle, called a *binary magnon-polaron* comprising a magnon, a phonon and another magnon.

We note that the experimentally measured value of the splitting frequency $2g$ is larger than the numerically simulated value, as shown in Fig. 3b. This difference could be because in our calculation, it was assumed that the

impedance mismatch between the voltage source and the sample caused the S_{11} parameter to be -0.2 dB, which was potentially an overestimation, and the actual reflection coefficient could be smaller; thus, much more power was launched into the SAW, causing the power to be transferred to the A1 mode from the source, and then, the power was transferred from the A1 mode to the $M1'$ and $M1''$ modes, producing a larger splitting frequency than in our simulation. In addition, the experiments were performed at room temperature, while the MuMax3 simulations were performed at $T = 0$ K. These reasons explain why the experimentally measured gap is larger than the numerically simulated gap.

The simulated spatial power and phase profiles of the $M1'$ and $M1''$ modes are shown in Fig. 3d at bias fields H_{ext} of 550 Oe (below the critical field where the strongest coupling occurs), 650 Oe (critical field) and 800 Oe (above the critical field). These are obtained by the method described in ref. ³⁵. The power profiles have the nature of center modes with the axis of symmetry canted from the major axis of the nanomagnets. This result is noticeably different from the profile in Fig. 2b, where no SAW (and hence no A1 mode due to the SAW) was present. Since it is A1 that couples $M1'$ and $M1''$, its presence is expected to change the power and phase profiles of both $M1'$ and $M1''$.

At the critical field of 650 Oe, the calculated phase profiles show azimuthally quantized behavior with a quantization number equal to 2. The phase profiles also show a 180° phase difference between $M1'$ and $M1''$, which is reminiscent of dark magnon modes³⁹. Because of this phase difference, the spins in the two spin wave modes $M1'$ and $M1''$ rotate in *opposite directions*, but it is not known which mode rotates clockwise and which mode rotates anti-clockwise. If we denote that clockwise rotating mode as $|C\rangle$ and the anti-clockwise rotating mode as $|A\rangle$, then the coupled mode can be written as $(1/\sqrt{2})(|C, A\rangle \pm |A, C\rangle)$, which cannot be written as any tensor product of the modes $|C\rangle$ and $|A\rangle$. This is reminiscent of some (but not all) of the features of Einstein–Podolsky–Rosen (entangled) states, with the exception of a classical system where there is no quantum non-locality since the coupled mode survives only in the presence of the coupling agent (the SAW) and vanishes immediately if the SAW is extinguished.

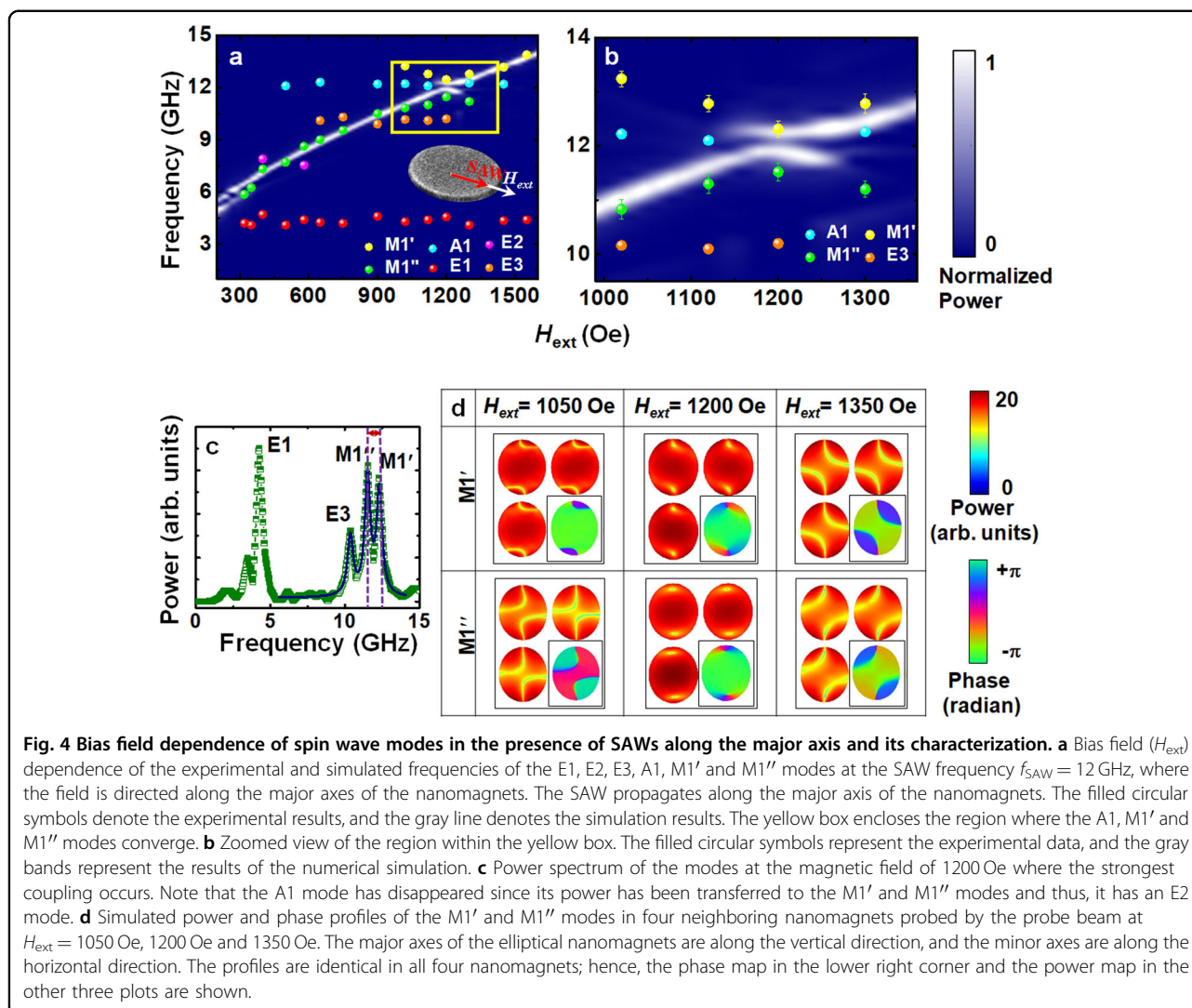
SAW propagating along the major axis of the nanomagnets

Because the nanomagnet array lacks rotational symmetry, we further studied the spin wave dynamics of the array with SAWs applied along the major axis of the elliptical nanomagnets instead of the minor axis. We also changed the SAW frequency from 9 to 12 GHz. At this frequency, good phase matching could occur again since the wave vectors of the acoustic wave and the resident spin wave within the nanomagnet match (see Section S4

of the Supplementary Material). Figure 4 shows the same data as Fig. 3, but for the case of the SAW propagating along the major axis of the nanomagnets instead of the minor axis; other details of the spectra are discussed in Sections S1 and S2 of the Supplementary Material.

The major difference from the case in Section 2.2.1 is that in addition to the magnetoelastic mode E1 (at 4.1 GHz) associated with laser heating and cooling and magnetoelastic mode A1 (12 GHz) associated with the SAW, there are two other magnetic-field-independent (hence magnetoelastic) modes E2 (7.5 GHz) and E3 (10 GHz). They have lower amplitudes than the other modes. Interestingly, the array pitch in the direction of SAW propagation, which is the center-to-center separation (a) between nearest neighbor nanomagnets, is 428 nm (Fig. 1b). The nanomagnets act as mechanical loads and can be viewed as distributed reflectors of the SAW. When the SAW wavelength matches the pitch, the reflected waves constructively interfere and build up, causing large acoustic power at that wavelength; this results in a strong magnetoelastic mode at the SAW frequency corresponding to that wavelength. If this is indeed the origin of mode E3, then the SAW frequency becomes 9.60 GHz: $f = v/\lambda = 4110/(428 \times 10^{-9}) = 9.60$ GHz, where v = velocity of SAW in LiNbO_3 substrate = 4110 m/s⁴⁰. The other magnetoelastic mode E2 corresponds to the SAW with the wave vector along the diagonal of the lattice⁴¹: $\lambda = \sqrt{a^2 + b^2} = 561 \text{ nm}$, where b is center to center separation along the minor axis and equal to 363 nm and f is defined as v/λ ($4110/(561 \times 10^{-9})$) and is equal to 7.32 GHz. These two frequencies of 9.6 and 7.32 GHz match reasonably well with those of E3 and E2, which are 10 and 7.5 GHz, respectively. If this is the origin of E2 and E3, these would be expected to appear when the SAW propagates parallel to the minor axes of the nanomagnets, but they do not. Thus, this explanation is only a speculation and not definitive.

In the case of the SAW propagating along the major axis, the maximum coupling occurs at a magnetic field of 1200 Oe, and as Fig. 4c shows, mode A1 has expectedly disappeared at that field since its power has been fully transferred to $M1'$ and $M1''$, characteristic of strong tripartite magnon-phonon-magnon coupling. The frequency gap at this magnetic field is $2g = 0.79 \pm 0.032$ GHz. The value of κ_1 , the spectral width of the $M1'$ mode, estimated at a magnetic field of 1350 Oe is 0.35 ± 0.028 GHz and the value of κ_2 , the spectral width of the $M1''$ mode, estimated at a magnetic field of 1050 Oe, is 0.37 ± 0.016 GHz; using these values, a cooperativity factor C ($C = g^2/\kappa_1\kappa_2$) of 1.20 is obtained. Again, these values of the cooperativity factor, g , and κ indicate that the coupling between $M1'$ and $M1''$ mediated by A1 barely falls in the *strong coupling* regime. Notably, this coupling is slightly weaker than the coupling that occurs when the SAW propagates along the minor axis



with a frequency of 12 GHz ($C = 1.39$; see Section S3 of the Supplementary Material). In the avoided crossing regime, where the two modes do not have their individual characteristics because of coupling, this value is ~ 0.77 ($C = g^2/\kappa^2$), where $g = 0.395 \pm 0.032$ GHz and $\kappa \sim 0.45$ GHz. Therefore, the strength of the coupling depends on the direction of propagation of the SAW with respect to the easy or hard axis of the nanomagnets, although the difference is not remarkably large. The difference occurs because the degree of phase matching that could be achieved is slightly different in the two cases.

Conclusion

In conclusion, we have demonstrated strong tripartite coupling involving two magnons and a phonon in a two-dimensional array of magnetostrictive nanomagnets on a piezoelectric substrate (a two-dimensional artificial magnetoelastic crystal) excited by a surface acoustic wave (SAW). The coupling occurs at magnetic fields where the

frequencies and wavevectors of the confined magnon modes in the nanomagnets match those of the SAW to ensure near-perfect phase matching between all modes. Phase matching can be ensured by engineering the SAW frequency, magnetic field and nanomagnet dimensions. This coupling transfers all or nearly all of the power from a magnetoelastic mode caused by the SAW to two Kittel-type spin wave modes. The associated cooperativity factor exceeded unity, indicating the formation of a binary magnon-polaron (magnon-phonon-magnon). Micro-magnetic simulations qualitatively reproduce the experimental observations. The coupling features show pronounced anisotropy since the nanomagnet array does not have rotational symmetry.

Methods

Sample fabrication

The LiNbO_3 substrate on which the magnetostrictive nanomagnets were fabricated was initially cleaned in

ethanol, and the Au electrodes for launching the SAW were delineated using optical lithography. After delineation of the electrodes, the substrate was spin-coated (spinning rate ~ 2500 rpm) with bilayer poly-methyl methacrylate (PMMA) resists of two different molecular weights and subsequently baked at 110°C for 5 min. Next, electron beam lithography was performed using a Hitachi SU-70 scanning electron microscope (SEM) with an accelerating voltage of 30 kV and beam current of 60 pA with a Nabyty NPGS lithography attachment to open windows for deposition of the nanomagnets. The resists were finally developed in methyl isobutyl ketone and isopropyl alcohol (MIBK-IPA, 1:3) for 270 s, followed by a cold IPA rinse. A 5-nm-thick Ti adhesion layer was deposited on the patterned substrate using an electron beam evaporation base pressure of $\sim 2 \times 10^{-7}$ Torr, followed by electron beam deposition of 6-nm-thick Co. Lift-off was carried out by removing the PG solution.

TR MOKE study

The polar Kerr rotation was measured by an optical bridge detector as a function of the time delay between the pump and probe beams using the TR-MOKE microscope. The sample was scanned by a piezoelectric x - y - z stage to position the pump and probe beams at the desired location of the sample. The probe spot was carefully placed at the center of the pump spot to measure the time-resolved dynamics from the uniformly excited region of the sample. A radio frequency (RF) signal from a signal generator (Rohde & Schwarz SMB100A, frequency range: 100 kHz to 20 GHz) was launched on the sample through a high-frequency and low noise coaxial cable (model no. N1501A-203).

Micromagnetic simulation

We performed micromagnetic simulations using MuMax3 software^{34,42}. For visualization of the simulated results, we used MuView software. In the simulation, we considered a 7×7 array of elliptical nanomagnets, discretizing the samples into rectangular prisms with dimensions of $2 \times 2 \times 6 \text{ nm}^3$.

In Figs. 3 and 4, we show a 2×2 nanomagnet array cropped from the center of the 7×7 array to eliminate edge effects. The cell size in the lateral plane was kept below the exchange length of cobalt to reproduce the observed magnetization dynamics. The magnetic parameters used for the simulation are as follows: saturation magnetization $M_s = 1300 \text{ emu/cm}^3$, gyromagnetic ratio $\gamma = 17.6 \text{ MHz/Oe}$, magneto-crystalline anisotropy field $H_k = 0$ (since the nanomagnets are amorphous or polycrystalline), and exchange stiffness constant $A_{ex} = 3.0 \times 10^{-5} \text{ erg/cm}$.

In the simulation, the external bias field H_{ext} was applied along the major axis of the nanomagnet to prepare the static micromagnetic distribution by allowing the

simulation to run for 1 ns (long enough to obtain a steady state). After 1 ns, the magnetization aligns along H_{ext} almost everywhere within the nanomagnet. The magnetization dynamics were triggered in the simulation using different excitation fields. The optical excitation was mimicked by a pulsed magnetic field excitation (peak amplitude = 20 Oe and pulse duration = 10 ps) perpendicular to the sample plane, whereas the effect of the SAW was mimicked by an additional sinusoidal anisotropy field by causing the strain anisotropy energy density to be equal to the following:

$$K(t) = K_0[\sin(2\pi ft)]; \quad K_0 = (3/2)\lambda_s\sigma \quad (2)$$

where f is the SAW frequency. Here, λ_s is the saturation magnetostriction, and σ is the amplitude of the sinusoidal time-varying stress due to the SAW. The stress was assumed to be uniaxial and applied along either the major or minor axis of the nanomagnet depending on whether the SAW was propagating along the major or minor axis. Since Co has negative magnetostriction, the compressive cycle of the stress tended to align the magnetization in the direction of the stress axis, and the tensile cycle tended to align the magnetization in the direction perpendicular to the stress axis.

To calculate the amplitude of the stress σ generated by the SAW, we follow the recipe⁴³ for a plane surface wave:

$$\sigma = \sqrt{2PZ_0}; \quad Z_0 = \sqrt{c_{11}P} \quad (3)$$

where P is the power in the wave per unit area, Z_0 is the characteristic acoustic impedance, c_{11} is the first diagonal element of the elasticity tensor and ρ is the mass density. The cross-sectional area through which the wave passes is the penetration depth times the width of the electrodes. The penetration depth is approximately the wavelength (which varies with the SAW frequency), but we take its average value to be $\sim 1 \mu\text{m}$ (which is the wavelength at $\sim 4 \text{ GHz}$ frequency). Therefore, the cross-sectional area of the wave is $\sim 1 \mu\text{m} \times 2 \text{ mm} = 2 \times 10^{-9} \text{ m}^2$. Since the power coupled into the substrate is 0.72 mW, the power per unit cross-sectional area P is 2.25 kW m^{-2} . For LiNbO_3 , $c_{11} = 202 \text{ GPa}$ and $\rho = 4650 \text{ kg m}^{-3}$. This yields $Z_0 = 9.7 \times 10^8 \text{ N s m}^{-3}$. Therefore, the stress generated is 19.6 MPa. There is a wide range in the reported values of the saturation magnetostriction of Co, λ_s ranging from 30 ppm⁴⁴ to 150 ppm⁴⁵. By using the higher value in view of the fact that magnetostriction may increase in nanomagnets⁴⁶, from Eq. (1), the amplitude of strain energy density (K_0) is calculated to be 4410 J/m^3 . In the simulation, we assumed it was 5000 J/m^3 since the estimate was probably accurate only to the order of magnitude.

The stress anisotropy acts as an effective magnetic field in the direction of the stress axis and is related to the

generated stress as follows:

$$H_{\text{stress}}(t) = K(t)/\mu_0 M_s = \left(\frac{3}{2}\right) \lambda_s \sigma \sin(2\pi ft) / \mu_0 M_s \quad (4)$$

where μ_0 is the magnetic permeability of free space and M_s is the saturation magnetization of the nanomagnets ($\sim 1.3 \text{ MA m}^{-1}$). The amplitude of the field value related to the peak strain anisotropy energy density is 39 Oe. Within each nanomagnet, the SAW amplitude is assumed to be spatially invariant, as is the amplitude of the effective magnetic field H_{stress} associated with it. The wavelength of the SAW in the frequency range of 1–10 GHz is a few hundred nanometers to a few micrometers in LiNbO_3 since the SAW velocity is 5–6 km/sec⁴⁷. The major axes of the nanomagnets are $\sim 360 \text{ nm}$, while the minor axes are $\sim 330 \text{ nm}$. Hence, at lower frequencies, the assumption of a spatially invariant H_{stress} amplitude is justified since the nanomagnet's lateral dimension is an order of magnitude smaller than the wavelength, but it is definitely questionable at higher frequencies. Since taking the spatial variation of the amplitude of H_{stress} into account would have been computationally prohibitive, we ignored this effect but understand that it could make some difference.

The micromagnetic simulations yield time-dependent magnetization components $M_x(x, y, z, t)$, $M_y(x, y, z, t)$, $M_z(x, y, z, t)$. From these components, we can calculate the spatial profiles shown in Figs. 2d, 3d and 4d using an in-house MATLAB code named “Dotmag”, described in ref. 35.

Acknowledgements

The authors would like to acknowledge the financial support from the Indo-US Science and Technology Fund Center Grant titled “Center for Nanomagnetism for Energy-Efficient Computing, Communications and Data Storage” (IUSSTF/JC-030/2018). A.B. gratefully acknowledges the financial support from the Department of Science and Technology (DST), Govt. of India under Grant No. DST/NM/TUE/QM-3/2019-1C-SNB. The work of S.B. is supported by the US National Science Foundation under grant ECCS-2235789. S.M. acknowledges S. N. Bose National Centre for Basic Sciences for Senior Research Fellowship. S.M. also acknowledges Anulekha De, Pratap Kumar Pal and Avinash Kumar Chaurasiya for assistance during TR-MOKE measurements.

Author contributions

A.B. planned and supervised the project. J.L.D. fabricated and performed initial characterization of the samples. S.M. fabricated the samples, performed the TRMOKE measurements and micromagnetic simulations and analyzed the results in consultation with A.B. S.M. and A.B. wrote the manuscript in consultation with all co-authors. S.B. assisted with editing the manuscript and interpretation of the results.

Data availability

All data needed to evaluate the conclusions in the manuscript are present in the manuscript and/or the Supplementary Materials. Additional data related to this study are available from the authors upon reasonable request.

Conflict of interest

The authors declare no competing interests.

Publisher's note

Springer Nature remains neutral with regard to jurisdictional claims in published maps and institutional affiliations.

Supplementary information The online version contains supplementary material available at <https://doi.org/10.1038/s41427-023-00499-4>.

Received: 7 January 2023 Revised: 20 July 2023 Accepted: 25 July 2023.

Published online: 29 September 2023

References

- Berk, C. et al. Strongly coupled magnon–phonon dynamics in a single nanomagnet. *Nat. Commun.* **10**, 2652 (2019).
- Vaclavkova, D. et al. Magnon polarons in the van der Waals antiferromagnet FePS_3 . *Phys. Rev. B* **104**, 134437 (2021).
- De, A. et al. Resonant amplification of intrinsic magnon modes and generation of new extrinsic modes in a two-dimensional array of interacting multiferroic nanomagnets by surface acoustic waves. *Nanoscale* **13**, 10016–10023 (2021).
- Fabiha, R. et al. Spin wave electromagnetic nano-antenna enabled by tripartite phonon-magnon-photon coupling. *Adv. Sci.* **9**, 2104644 (2022).
- Drobitch, J. L. et al. Extreme subwavelength magnetoelastic electromagnetic antenna implemented with multiferroic nanomagnets. *Adv. Mater. Technol.* **5**, 2000316 (2020).
- Mondal, S. et al. Hybrid magnetodynamical modes in a single magnetostriptive nanomagnet on a piezoelectric substrate arising from magnetoelastic modulation of precessional dynamics. *ACS Appl. Mater. Interfaces* **10**, 43970–43977 (2018).
- Yang, W.-G. & Schmidt, H. Acoustic control of magnetism toward energy-efficient applications. *Appl. Phys. Rev.* **8**, 021304 (2021).
- Kamra, A. & Bauer, G. E. W. Actuation, propagation, and detection of transverse magnetoelastic waves in ferromagnets. *Solid State Commun.* **198**, 35–39 (2014).
- Godejohann, F. et al. Magnon polaron formed by selectively coupled coherent magnon and phonon modes of a surface patterned ferromagnet. *Phys. Rev. B* **102**, 144438 (2020).
- Simensen, H. T., Troncoso, R. E., Kamra, A. & Brataas, A. Magnon-polarons in cubic collinear antiferromagnets. *Phys. Rev. B* **99**, 064421 (2019).
- Li, J. et al. Observation of magnon polarons in a uniaxial antiferromagnetic insulator. *Phys. Rev. Lett.* **125**, 217201 (2020).
- Streib, S., Vidal-Silva, N., Shen, K. & Bauer, G. E. Magnon-phonon interactions in magnetic insulators. *Phys. Rev. B* **99**, 184442 (2019).
- Kikkawa, T. et al. Magnon polarons in the spin Seebeck effect. *Phys. Rev. Lett.* **117**, 207203 (2016).
- Pimenov, A. et al. Possible evidence for electromagnons in multiferroic manganites. *Nat. Phys.* **2**, 97–100 (2006).
- Vidal-Silva, N., Aguilera, E., Roldán-Molina, A., Duine, R. & Nunez, A. Magnon polarons induced by a magnetic field gradient. *Phys. Rev. B* **102**, 104411 (2020).
- Hashimoto, Y. et al. Frequency and wavenumber selective excitation of spin waves through coherent energy transfer from elastic waves. *Phys. Rev. B* **97**, 140404 (2018).
- Babu, N. K. et al. The interaction between surface acoustic waves and spin waves: The role of anisotropy and spatial profiles of the modes. *Nano Lett.* **21**, 946–951 (2020).
- Yang, W., Jaris, M., Hibbard-Lubow, D., Berk, C. & Schmidt, H. Magnetoelastic excitation of single nanomagnets for optical measurement of intrinsic Gilbert damping. *Phys. Rev. B* **97**, 224410 (2018).
- Yang, W., Jaris, M., Berk, C. & Schmidt, H. Preferential excitation of a single nanomagnet using magnetoelastic coupling. *Phys. Rev. B* **99**, 104434 (2019).
- Jaris, M., Yang, W., Berk, C. & Schmidt, H. Towards ultraefficient nanoscale straintronic microwave devices. *Phys. Rev. B* **101**, 214421 (2020).
- Yang, W.-G. & Schmidt, H. Greatly enhanced magneto-optic detection of single nanomagnets using focused magnetoelastic excitation. *Appl. Phys. Lett.* **116**, 212401 (2020).
- Yahagi, Y., Harteneck, B., Cabrini, S. & Schmidt, H. Controlling nanomagnet magnetization dynamics via magnetoelastic coupling. *Phys. Rev. B* **90**, 140405 (2014).
- Kittel, C. Interaction of spin waves and ultrasonic waves in ferromagnetic crystals. *Phys. Rev.* **110**, 836 (1958).

24. Akhiezer, A., Bar'lakhtar, V. & Peletminskii, S. Coupled magnetoelastic waves in ferromagnetic media and ferroacoustic resonance. *J. Sov. Phys. JETP* **35**, 157 (1959).
25. Tucker, J. W. & Rampton, V. *Microwave Ultrasonics in Solid State Physics* (North-Holland, 1973).
26. Scherbakov, A. et al. Coherent magnetization precession in ferromagnetic (Ga, Mn) As induced by picosecond acoustic pulses. *Phys. Rev. Lett.* **105**, 117204 (2010).
27. Weiler, M. et al. Elastically driven ferromagnetic resonance in nickel thin films. *Phys. Rev. Lett.* **106**, 117601 (2011).
28. Kim, J.-W., Vomir, M. & Bigot, J.-Y. Ultrafast magnetoacoustics in nickel films. *Phys. Rev. Lett.* **109**, 166601 (2012).
29. Kittel, C. On the theory of ferromagnetic resonance absorption. *Phys. Rev.* **73**, 155 (1948).
30. Zhao, C. et al. Direct imaging of resonant phonon-magnon coupling. *Phys. Rev. Appl.* **15**, 014052 (2021).
31. Casals, B. et al. Generation and imaging of magnetoacoustic waves over millimeter distances. *Phys. Rev. Lett.* **124**, 137202 (2020).
32. Rana, B. et al. Detection of picosecond magnetization dynamics of 50 nm magnetic dots down to the single dot regime. *ACS nano* **5**, 9559–9565 (2011).
33. Barman, A. & Sinha, J. *Spin Dynamics and Damping in Ferromagnetic Thin Films and Nanostructures*. (Springer, 2018).
34. Vansteenkiste, A. et al. The design and verification of MuMax3. *AIP Adv.* **4**, 107133 (2014).
35. Kumar, D., Dmytriiev, O., Ponraj, S. & Barman, A. Numerical calculation of spin wave dispersions in magnetic nanostructures. *J. Phys. D: Appl. Phys.* **45**, 015001 (2011).
36. Pierce, J. R. Coupling of modes of propagation. *J. Appl. Phys.* **25**, 179–183 (1954).
37. Miller, S. E. Coupled wave theory and waveguide applications. *Bell Syst. Tech. J.* **33**, 661–719 (1954).
38. Chen, J. et al. Strong interlayer magnon-magnon coupling in magnetic metal-insulator hybrid nanostructures. *Phys. Rev. Lett.* **120**, 217202 (2018).
39. Zhang, X. et al. Magnon dark modes and gradient memory. *Nat. Commun.* **6**, 1–7 (2015).
40. Holm, A., Stürzer, Q., Xu, Y. & Weigel, R. Investigation of surface acoustic waves on LiNbO₃, quartz, and LiTaO₃ by laser probing. *Microelectron. Eng.* **31**, 123–127 (1996).
41. Giannetti, C. et al. Thermomechanical behavior of surface acoustic waves in ordered arrays of nanodisks studied by near-infrared pump-probe diffraction experiments. *Phys. Rev. B* **76**, 125413 (2007).
42. Sahoo, S. et al. Observation of coherent spin waves in a three-dimensional artificial spin ice structure. *Nano Lett.* **21**, 4629–4635 (2021).
43. Datta, S. *Surface Acoustic Wave Devices* (Prentice Hall, 1986).
44. Nishiyama, Z. On the magnetostriction of single crystals of cobalt. *Sci. Rep. Tohoku Imp. Univ.* **18**, 341 (1929).
45. Bozorth, R. Magnetostriction and crystal anisotropy of single crystals of hexagonal cobalt. *J. Phys. Rev.* **96**, 311 (1954).
46. Zhao, S. Advances in multiferroic nanomaterials assembled with clusters. *J. Nanomater.* **2015**, 1–12 (2015).
47. Shibata, Y. et al. Epitaxial growth and surface acoustic wave properties of lithium niobate films grown by pulsed laser deposition. *J. Appl. Phys.* **77**, 1498–1503 (1995).